

Exploring bosonic and fermionic link models on $(3 + 1)$ D tubesDebasish Banerjee^{1,2}, Emilie Huffman³, and Lukas Rammelmüller^{4,5}¹Theory Division, Saha Institute of Nuclear Physics, HBNI, 1/AF Bidhannagar, Kolkata 700064, India²Homi Bhabha National Institute, Training School Complex, Anushaktinagar, Mumbai 400094, India³Perimeter Institute for Theoretical Physics, 31 Caroline Street North, Waterloo, Ontario, Canada N2L 2Y5⁴Arnold Sommerfeld Center for Theoretical Physics (ASC), University of Munich, Theresienstr. 37, 80333 München, Germany⁵Munich Center for Quantum Science and Technology (MCQST), Schellingstr. 4, 80799 München, Germany

(Received 1 March 2022; accepted 12 July 2022; published 2 September 2022)

Quantum link models have attracted a lot of attention in recent times as a generalization of Wilson's lattice gauge theories, and are particularly suitable for realization on quantum simulators and computers. These models are known to host new phases of matter and act as a bridge between particle and condensed matter physics. In this paper, we study the Abelian $U(1)$ lattice gauge theory in $(3 + 1)$ D tubes using large-scale exact diagonalization. We are then able to motivate the phase diagram of the model with finite-size scaling techniques, and in particular propose the existence of a Coulomb phase. Furthermore, we introduce models involving *fermionic quantum links*, which generalize the gauge degrees of freedom to be of fermionic nature. We prove that while the spectra remain identical between the bosonic and the fermionic versions of the $U(1)$ -symmetric quantum link models in $(2 + 1)$ D, they are different in $(3 + 1)$ D. We discuss the prospects of realizing the magnetic field interactions as correlated hopping in quantum simulator experiments.

DOI: [10.1103/PhysRevResearch.4.033174](https://doi.org/10.1103/PhysRevResearch.4.033174)

I. INTRODUCTION

Gauge theories have a formidable legacy in the description of naturally occurring matter. Examples of their diverse applications include *ab initio* descriptions of the strong interaction phenomenology in particle physics, which use quantum chromodynamics (QCD) as the starting point, and descriptions of superconductivity in condensed matter physics, which use $U(1)$ gauge fields to bind electrons. Even the Kitaev model, which is used to introduce topological quantum computation, is a \mathbb{Z}_2 lattice gauge theory. Naturally, many of these gauge theories need to couple the fundamental degrees of freedom very strongly, which in turn renders weak-coupling perturbation theory useless. Wilson [1] pioneered the technique of discretizing the gauge theories nonperturbatively on a space-time lattice and the use of Markov chain Monte Carlo methods to sample the resulting path integral. This approach has been developed to a high degree of sophistication, where many aspects of particle physics and condensed matter phenomenology can be directly studied *ab initio* using Monte Carlo simulations [2].

While in the Wilsonian approach, one discretizes the gauge field action via the parallel transporters which live on the links of a lattice, it is also possible to approach the problem from a Hamiltonian perspective. The latter approach [3] is

particularly useful when one wants to address gauge theories using the novel tools of quantum simulators and quantum computers. Quantum computing is a rapidly developing computing paradigm using the notions of quantum entanglement, and can in principle highly outperform classical computing paradigms (such as Markov chain Monte Carlo) in certain parameter regimes [4]. Such regimes occur in strongly correlated systems for unitary evolution of the system in real time, at finite density, or with background electric and magnetic fields.

In the Hamiltonian formulation of Wilson's lattice gauge theories for compact $U(1)$ or $SU(2)$ gauge groups, one has to deal with a locally infinite-dimensional Hilbert space even for single-link degrees of freedom. This makes it tricky to use this formulation for quantum computation, which naturally has a finite number of available states. Imposing a naive cutoff on the number of allowed states risks breaking gauge invariance. Remarkably, it is possible to define gauge theories that have finite-dimensional Hilbert spaces, and yet still possess these continuous gauge symmetries, by judiciously using nonunitary link operators. Quantum link models (QLMs), as they are called, have been theoretically developed to possess both Abelian and non-Abelian local symmetries [5–7], including QCD [8]. Qubit-regularized quantum field theories (QFTs), which generalize the construction of QFTs using discrete degrees of freedom, are being actively investigated [9,10]. Such formulations have also been used in condensed matter physics in the context of superconductivity [11,12] and frustrated magnetism [13]. Only recently have the connections between the corresponding microscopic theories been fully appreciated, and exploited to better understand the underlying physics of the systems. The fact that they have a finite-dimensional Hilbert space of the gauge degrees of

Published by the American Physical Society under the terms of the [Creative Commons Attribution 4.0 International](https://creativecommons.org/licenses/by/4.0/) license. Further distribution of this work must maintain attribution to the author(s) and the published article's title, journal citation, and DOI.



FIG. 1. A schematic phase diagram of the U(1) quantum link model with the spin and fermionic representation as a function of the coupling λ . For large negative λ , there is a nematically ordered phase which spontaneously breaks the lattice (rotation) symmetries. For small values of λ , the broken symmetry is restored. For $\lambda \rightarrow 1$, the winding fluxes can be excited easily and additionally for the fermionic model there is a narrow region where they become the ground state, before hitting the Rokhsar-Kivelson point at $\lambda = 1$.

freedom, and yet still possess the same local symmetry as the Wilson-type models, makes them attractive candidates as models to be implemented in quantum computers, or quantum simulators.

While it is established that these QLMs can be set up to have the same continuous gauge symmetries as the Wilson-type theories, there remain many open questions as to the nature of the phases that this family of gauge theories can host. Since they are generalized lattice gauge theories, they certainly give rise to novel phases which cannot be realized on Wilson-type theories. As a classic example, U(1) QLMs in $(2+1)$ D give rise to phases where electric flux tubes joining static charges are fractionalized in units of $\frac{1}{2}$ or even $\frac{1}{4}$ [14,15]. However, whether QLMs in higher dimensions can support deconfined Coulomb phases like continuum gauge fields is still an open question. A resolution of this question would certainly boost the importance of QLMs for consideration in quantum simulator experiments.

Interestingly, the same question is also of prime importance in condensed matter physics, where existence of the Coulomb phase is a key ingredient to postulate the existence of quantum spin liquids, a phase of matter which does not break any internal or lattice symmetries and has fractionalized excitations. Previous work has already provided indications that this might indeed be the case [16–19]. In this paper, using large-scale exact diagonalization on the U(1) QLM on the cubic lattice and techniques of finite-size scaling, we provide evidence of a region in the parameter space where the ground state does not break any symmetries, lattice or internal, and the system is gapped. A schematic of the phases we propose can be found in the “bosons” side of Fig. 1. Since we are severely restricted to small lattice sizes, our results should also encourage the development of novel algorithms to address the system on large lattices, or perhaps quantum simulator experiments. Should the different computational methods be able to establish the existence of a Coulomb phase in these models, it would be of fundamental importance in the context of quantum field theories as well. We would thus have demonstrated an intriguing

way to generate a massless gauge boson from a microscopic theory with a finite-dimensional Hilbert space.

As an important conceptual development, we also extend the same ideas which inspired the quantum link formulation to introduce a different kind of quantum link model, where the gauge link operators are represented by fermionic creation and annihilation operators. We emphasize that this construction is distinct from the rishon representation [8,20], where the quantum link operators are represented as fermionic bilinear operators, such that all commutation relations are preserved. We establish that the gauge invariance in the model is a consequence of the special type of correlated subdimensional hopping of the fermionic particles living on the links, and thus connected to similar ideas in the models of fractons. Using geometric constructions, we show that in $(2+1)$ D, the spectra of the fermions and quantum spins $S = \frac{1}{2}$ are identical, while in $(3+1)$ dimensions $[(3+1)$ D] they differ due to the Pauli exclusion principle. Using ED studies, we also offer a first glimpse into the phase diagram of the fermionic model in $(3+1)$ D, which we sketch in the “fermions” side of Fig. 1. One expects that any reasonably efficient quantum Monte Carlo method that can be made to work for the spin model would suffer a severe sign problem for the fermionic version [21], so we outline the possibility of realizing this Hamiltonian on an analog quantum simulator platform.

II. MODELS AND SYMMETRIES

We begin our presentation by describing the microscopic models and the symmetries of the system. We also motivate how these models can be applied to naturally occurring phenomena in particle and condensed matter physics. For an overview of the physics, we provide a phase diagram for the models proposed in Fig. 1.

A. Bosonic quantum link model

We first introduce the conventional bosonic version of an U(1) Abelian QLM. While these models can be studied on any lattice on which loops can be defined, we consider square and cubic lattices for concreteness. The operators of the gauge theory are defined on the links joining two adjacent lattice sites. The Hamiltonian of the link model is

$$H = \frac{g^2}{2} \sum_{x,\mu} E_{x,\mu}^2 - J \sum_{\square} (U_{\square} + U_{\square}^{\dagger}) + \lambda \sum_{\square} (U_{\square} + U_{\square}^{\dagger})^2, \quad (1)$$

where $E_{x,\mu}$ is the electric field operator defined on the link joining the sites x and $x + \hat{\mu}$. The first term is the electric field energy, the second term expressed via plaquettes is the magnetic field energy, and the third term is the Rokhsar-Kivelson (RK) term. The plaquette operator U_{\square} is defined via the parallel transport operator $U_{x,\mu}$ as

$$U_{\square} = U_{x,\mu} U_{x+\hat{\mu},\nu} U_{x+\hat{\nu},\mu}^{\dagger} U_{x,\nu}^{\dagger}. \quad (2)$$

Each link has three operators $U_{x,\mu}$, $U_{x,\mu}^{\dagger}$, and $E_{x,\mu}$ which can be realized by the generators of an $\text{SU}(2)$ algebra. The

operators satisfy the following commutation relations:

$$\begin{aligned}
 [E_{x,\mu}, U_{y,v}] &= U_{x,\mu} \delta_{x,y} \delta_{\mu,v}, \\
 [E_{x,\mu}, U_{y,v}^\dagger] &= -U_{x,\mu}^\dagger \delta_{x,y} \delta_{\mu,v}, \\
 [U_{x,\mu}, U_{y,v}^\dagger] &= 2E_{x,\mu} \delta_{x,y} \delta_{\mu,v}.
 \end{aligned}
 \tag{3}$$

The Hamiltonian has a local U(1) invariance generated by the lattice Gauss-law operator

$$G_x = \sum_{\mu} (E_{x,\mu} - E_{x-\hat{\mu},\mu}),
 \tag{4}$$

with the local commutation relations

$$[G_x, H] = 0 \quad \text{for all } x.
 \tag{5}$$

This necessitates the specification of additional conditions to define the superselection sector of the Hilbert space by specifying the local charges. In the context of particle physics, it is usual to choose a vacuum which does not have any charges. Mathematically, this is expressed as $G_x|\psi\rangle = 0$, where $|\psi\rangle$ is a physical state of the theory. It is, of course, possible to choose various other superselection sectors by specifying different charges on different sites. An example is the quantum dimer model, a model to describe the non-Néel phases of quantum antiferromagnets relevant to high- T_c superconductivity. This model works with a different superselection sector, mathematically represented as $G_x|\chi\rangle = (-1)^x|\chi\rangle$, where $(-1)^x$ is the site parity.

Using the infinitesimal generators G_x , one can generate a finite unitary transformation $V = \prod_x e^{-i\theta_x G_x}$, where $\theta_x \in (0, 2\pi]$ are local parameters. Then, under the gauge transformations, the spectrum and the eigenstates $|\psi\rangle$ remain unchanged, irrespective of their degeneracies:

$$H|\psi\rangle = E|\psi\rangle \Rightarrow VHV^\dagger V|\psi\rangle = E|\psi\rangle,
 \tag{6}$$

which follows from Eq. (4). Note that any representation of the operators $E_{x,\mu}$, $U_{x,\mu}$, and $U_{x,\mu}^\dagger$ is admissible as long as the commutation relations in Eq. (3) are satisfied. The well-known case of Wilson-type lattice gauge theory uses the quantum rotor as a degree of freedom, generating an infinite-dimensional representation on each of the links. In this case, $U_{x,\mu}$ is an unitary operator, and the commutation relation between $U_{x,\mu}$ and $U_{x,\mu}^\dagger$ vanishes. This is a special feature of the Wilson theory, which immediately narrows down the possible physical scenarios.

Interestingly, a finite-dimensional representation of the gauge fields can be obtained using quantum spin- S operators $\hat{S}_{x,\mu}$. In particular, the raising and the lowering spin operators can be identified with the quantum link gauge fields, and the z component with the electric field:

$$U_{x,\mu} = S_{x,\mu}^+; \quad U_{x,\mu}^\dagger = S_{x,\mu}^-; \quad E_{x,\mu} = S_{x,\mu}^z.
 \tag{7}$$

Note that viewed this way, one way of approaching the Wilson limit of the gauge theory is to consider larger-spin representations [22,23].

It is possible to give a pictorial representation of the QLM, which we show for the case of spin $S = \frac{1}{2}$. It is easiest to work in the electric flux basis, and the local Hilbert space is two dimensional. We can represent left- and right-pointing arrows on the horizontal links as well as top- and bottom-pointing

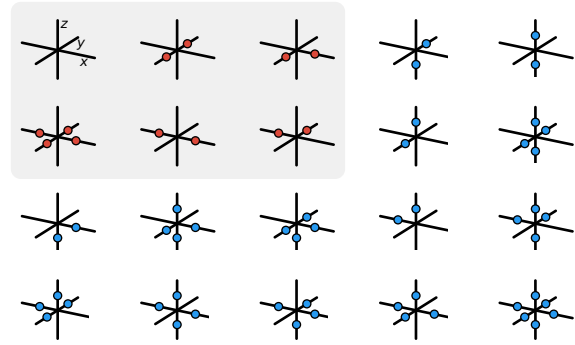


FIG. 2. Gauss-law compatible states. In total there are 20 allowed states for a 3D cubic lattice, and the gray-shaded area highlights the six compatible states for a 2D square lattice (where the z component is neglected).

arrows on the vertical links to denote $\frac{1}{2}$ and $-\frac{1}{2}$, respectively. These considerations allow us to write the Hamiltonian of the U(1) QLM in a more pictorial representation:

$$\begin{aligned}
 \hat{H} = -J \sum_{\square} & \left(\left| \begin{array}{c} \square \\ \leftarrow \end{array} \right\rangle \left\langle \begin{array}{c} \square \\ \rightarrow \end{array} \right| + \left| \begin{array}{c} \square \\ \rightarrow \end{array} \right\rangle \left\langle \begin{array}{c} \square \\ \leftarrow \end{array} \right| \right) \\
 + \lambda \sum_{\square} & \left(\left| \begin{array}{c} \square \\ \uparrow \end{array} \right\rangle \left\langle \begin{array}{c} \square \\ \downarrow \end{array} \right| + \left| \begin{array}{c} \square \\ \downarrow \end{array} \right\rangle \left\langle \begin{array}{c} \square \\ \uparrow \end{array} \right| \right).
 \end{aligned}
 \tag{8}$$

For the spin- $\frac{1}{2}$ case, the electric field energy terms contribute a constant and can be ignored. This corresponds to setting $g^2 = 0$, which we will consider for the rest of the paper.

It is instructive to point out that it is also possible to give a *particle* interpretation of the spin directions, such that $E = +\frac{1}{2}$ indicates the presence of a hard-core boson, and $E = -\frac{1}{2}$ the absence of the particle. Then, the above pictorial Hamiltonian corresponds to

$$\begin{aligned}
 \hat{H} = -J \sum_{\square} & \left(\left| \begin{array}{c} \bullet \\ \square \\ \leftarrow \end{array} \right\rangle \left\langle \begin{array}{c} \square \\ \bullet \\ \rightarrow \end{array} \right| + \left| \begin{array}{c} \square \\ \bullet \\ \rightarrow \end{array} \right\rangle \left\langle \begin{array}{c} \square \\ \bullet \\ \leftarrow \end{array} \right| \right) \\
 + \lambda \sum_{\square} & \left(\left| \begin{array}{c} \bullet \\ \square \\ \uparrow \end{array} \right\rangle \left\langle \begin{array}{c} \square \\ \bullet \\ \downarrow \end{array} \right| + \left| \begin{array}{c} \square \\ \bullet \\ \downarrow \end{array} \right\rangle \left\langle \begin{array}{c} \square \\ \bullet \\ \uparrow \end{array} \right| \right).
 \end{aligned}
 \tag{9}$$

This illustrates how Gauss' law constrains the Hilbert space. For a hypercubic lattice, four links touch a site in two spatial dimensions, while six links touch a site in three spatial dimensions. Normally, this would have given rise to $2^4 = 16$ states in the former case, and $2^6 = 64$ states in the latter case. With Gauss' law, this would allow only six states in two dimensions, and 20 states in three dimensions. Their particle representation is sketched in Fig. 2.

B. Fermionic quantum link model

Motivated by the particle representation, we introduce a different class of Abelian QLMs. This class of models follows immediately from the particle formulation of QLMs in the previous section if one postulates that the particle is a

fermion. This has the additional implication that the different link operators must also anticommute, in addition to the first two commutation relations of Eq. (3), which are necessary for the gauge invariance of any microscopic model.

Mathematically, we postulate that the two-dimensional Hilbert space at each link consists of two states: the absence or the presence of a fermion on the link. In the fermion occupation number basis, we can denote the two possibilities as $|0\rangle$ and $|1\rangle = c_{x,\mu}^\dagger |0\rangle$, respectively. Here $c_{x,\mu}^\dagger$ is a fermionic creation operator on the link joining the sites x and $x + \hat{\mu}$. Similarly, $|0\rangle = c_{x,\mu} |1\rangle$, where $c_{x,\mu}$ is an annihilation operator. Since fermionic creation and annihilation operators anticommute we have $c_{x,\mu} c_{x,\mu}^\dagger = 1 - c_{x,\mu}^\dagger c_{x,\mu}$, and we can write $|0\rangle = c_{x,\mu} |1\rangle = c_{x,\mu} c_{x,\mu}^\dagger |0\rangle = (1 - c_{x,\mu}^\dagger c_{x,\mu}) |0\rangle$, so that we can interpret the number operator as $n_{x,\mu} = c_{x,\mu}^\dagger c_{x,\mu}$. At this point, the similarities are obvious so that we can identify the number operator as the electric field, and the creation and the annihilation operators as the quantum link and its Hermitian conjugate:

$$U_{x,\mu} = c_{x,\mu}^\dagger, \quad U_{x,\mu}^\dagger = c_{x,\mu}, \quad E_{x,\mu} = n_{x,\mu} - \frac{1}{2}. \quad (10)$$

Note that with this identification the electric flux is still a bosonic operator, as is expected of a physical operator representing the electric field. The $\frac{1}{2}$ gives the electric flux the same values as a quantum spin $S = \frac{1}{2}$. The success of this identification of the operators is due to the fact that the creation and the annihilation operators satisfy the exact same commutation relations as the spin- $\frac{1}{2}$ operators:

$$\begin{aligned} [n_{x,\mu}, c_{y,v}^\dagger] &= c_{x,\mu}^\dagger \delta_{x,y} \delta_{\mu,v}, \\ [n_{x,\mu}, c_{y,v}] &= c_{x,\mu} \delta_{x,y} \delta_{\mu,v}, \\ [c_{x,\mu}^\dagger, c_{y,v}] &= 2E_{x,\mu} \delta_{x,y} \delta_{\mu,v} = 2(n_{x,\mu} - \frac{1}{2}) \delta_{x,y} \delta_{\mu,v}. \end{aligned} \quad (11)$$

The quantum link operators themselves satisfy the anticommutation relations:

$$\begin{aligned} \{c_{x,\mu}, c_{y,v}\} &= \{c_{x,\mu}^\dagger, c_{y,v}^\dagger\} = 0, \\ \{c_{x,\mu}^\dagger, c_{y,v}\} &= \delta_{x,y} \delta_{\mu,v}. \end{aligned} \quad (12)$$

The introduction of the fermionic operators is the key feature of this class of QLMs. The fermionic world lines have nonlocal correlations due to the Pauli exclusion principle, and we expect qualitatively different phenomena to occur with fermionic links, beyond the ones realized in the bosonic version, and certainly beyond the ones in Wilson-type gauge theories.

It is useful to note immediately that this proposed representation is very different from the rishon representations already motivated in [8] and used in [20] for atomic quantum simulators. Note that the rishons are a generalization of the Schwinger boson construction, in which each link has a fixed number of fictitious particles called rishons, the number of which is determined by the representation. In an appropriately chosen basis, each quantum link operator essentially shifts the positions of the particles on a link. Additionally, there is an emergent link $U(1)$ gauge symmetry with the rishons, corresponding to the total number of rishons on a link. In contrast, the particle representation introduced here does not keep the total number of particles fixed within a link, but only

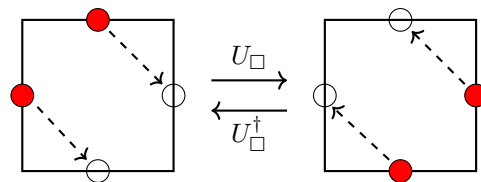


FIG. 3. Correlated particle hop. The term U_\square (or U_\square^\dagger) involving fermionic operators can be understood as a simultaneous hop of the fermionic particles within the plaquette along the dashed lines. The solid lines show the action of U_\square (from the left state to the right state) and U_\square^\dagger (from the right state to the left state), respectively.

globally. The particles, whether bosonic or fermionic, are free to move about on the lattice.

In terms of the fermionic operators, we can now write the plaquette and local operators as

$$\begin{aligned} U_\square &= c_{x,i}^\dagger c_{x+\hat{i},j}^\dagger c_{x+\hat{j},i} c_{x,j}, \\ G_x &= \sum_i (n_{x,\hat{i}} - n_{x-\hat{i},\hat{i}}). \end{aligned} \quad (13)$$

We note that due to the anticommutation properties of the fermionic operators, the order of the operators matters and the theory will not be fully defined until the operator ordering for the states in the Hilbert space is defined. The plaquette operator is composed of two creation and two annihilation operators, and this works out to be a correlated hop of two fermions, as shown in Fig. 3. This particular type of correlated hopping has peculiar consequences, as will be explained in Sec. IV. In particular, note that not all kinds of hoppings are possible, and this is the manifestation of the constraint, consistent with Gauss' law. The only allowed hoppings are when shaded sites are occupied and their directed neighbors are empty, in which case both the hoppings are oriented in the same direction. Thus, among the six possible hoppings, only two are actually allowed. It can be shown (via a unitary transformation) that the resulting theory is identical if the two hoppings instead occur in reverse directions.

III. METHODS

In this section, we discuss the symmetries of the model under study as well as the employed methodology. As mentioned previously, our main approach is the numerical diagonalization of Eq. (8) on 3D lattices (with an even extent in all directions) up to 48 links ($2 \times 2 \times 4$). To this end, we employ the Lanczos algorithm [24] to extract a portion of the low-lying energy spectrum as well as the ground-state wave function. Moreover, we discuss a systematic approximation, which we use for larger systems up to 96 links ($2 \times 2 \times 6$). Systems above 48 links are out of reach for full diagonalization for our current numerical implementation. A crucial ingredient for both approaches is to efficiently construct the Hilbert space by finding all permissible Gauss' law states (GLS) on a given lattice. For completeness, we describe our algorithm in Appendix A, where we also briefly discuss the steep scaling of the number of GLS with lattice size.

A. Symmetries of the microscopic model

The Hamiltonian in Eq. (8) features several global symmetries, which we may use to reduce the computational burden by separately diagonalizing the blocks corresponding to the different quantum numbers associated with the symmetries. Below, we explain these symmetries and how they are implemented for the bosonic and the fermionic representations.

The overwhelming advantage arises from exploiting the conservation of the winding numbers in a given plane under plaquette flips in this plane. On a 3D lattice, there are three such separately conserved winding numbers, generating a $U(1) \otimes U(1) \otimes U(1)$ symmetry and mathematically expressed as

$$W_x = \frac{1}{L_y L_z} \sum_{i,x=x_0} E_{i,\hat{x}}, \quad (14)$$

$$W_y = \frac{1}{L_x L_z} \sum_{i,y=y_0} E_{i,\hat{y}}, \quad (15)$$

$$W_z = \frac{1}{L_x L_y} \sum_{i,z=z_0} E_{i,\hat{z}}. \quad (16)$$

For a pictorial representation of the winding numbers on a $2 \times 2 \times 2$ lattice see Fig. 15. In the particle representation, recall that the $E_{i,\mu}$ operators should be replaced by $n_{i,\mu} - \frac{1}{2}$ since the occupation numbers can be only 0 or 1. This puts the E -flux values to be in one-to-one correspondence with the original formulation using spin $\frac{1}{2}$. In this notation, the winding number in each direction can go from $-L_\mu/2$ to $L_\mu/2$, thus resulting in a total of $(L_x + 1) \times (L_y + 1) \times (L_z + 1)$ sectors for a lattice with even (L_x, L_y, L_z) extents. For any lattice, the $W = [W_x W_y W_z] = [000]$ winding sector will be the largest block and is *a priori* expected to host the ground state, being the most symmetric configuration.

The Hamiltonian has a \mathbb{Z}_2 charge-conjugation symmetry. The unitary transformation is implemented on an operator \mathcal{O} as ${}^C\mathcal{O} = C\mathcal{O}C^\dagger$. In the original formulation with quantum spins, this yields ${}^C U = U^\dagger$; ${}^C U^\dagger = U$; ${}^C E = -E$. For the spin representation (which is equivalent to the hard-core boson representation), the charge-conjugation operator is $C = \sigma^x$. In the fermion representation, in terms of the creation and annihilation operators acting on individual links we have $C = (c^\dagger + ic)$. Using the fermion anticommutators (or the Pauli matrices for the spins), it is easy to show that $C^\dagger C = 1 = C^2$. For the fermions, additional phases are involved in the transformation of the individual link operators, but the observable electric flux transforms as in the spin representation:

$$\begin{aligned} {}^C c^\dagger &= ic; & {}^C c &= -ic^\dagger; \\ {}^C (n - \frac{1}{2}) &= -(n - \frac{1}{2}). \end{aligned} \quad (17)$$

To define the transformation on the entire system, or on the wave function, an ordering of the links on the lattice needs to be chosen and the product of individual transformations taken along the ordering:

$$C = \prod_{i=1}^{N_s} [c_i^\dagger + ic_i]. \quad (18)$$

For the spin representation, this works out to be a product of σ^x on all links, while for the hard-core bosons use bosonic creation and annihilation operators which commute for unequal

sites, but anticommute for identical sites [25]. Obviously, the ordering is not important for the spins or the hard-core bosons. At the single-plaquette level, the Hermitian conjugate of the plaquette-flip operator U_\square is U_\square^\dagger , and is identical to the charge-conjugation operation. Similarly, it is easy to see that in the absence of any matter, Gauss' law is also satisfied under charge conjugation. Note that this transformation preserves the commutation relation of the quantum spins, as well as the anticommutation relations of the fermions.

Similarly, the Hamiltonian is invariant under parity transformations, which can be defined as for the fermionic representation:

$$P = \prod_{i=1}^{N_s} [c_{P(i)}^\dagger + ic_{P(i)}], \quad (19)$$

where $P(i)$ simply denotes the point reflected index around the origin (with appropriately imposed periodic boundary conditions). Note that under the parity operation, the links and the flux transforms as ${}^P U_{xy} \rightarrow U_{-y,-x}^\dagger$; ${}^P E_{xy} \rightarrow -E_{xy}$.

In addition, the model has the other point-group symmetries, such as translation invariance (in each of the x , y , and z directions), the rotation symmetries (the C_4 rotations about the lattice axes, the C_3 rotations about the body diagonals, the C_2 rotations about the axis joining the opposite edges) the subscript n denotes the $(2\pi/n)$ -fold rotation. While it is possible to take advantage of the commuting symmetries to increase the numerical reach of our exact diagonalization routines, we have not considered it here.

B. Low-energy approximation

Because of the prohibitive scaling of the number of GLS with system size (see Appendix A for a discussion), ED is restricted to the lowest system sizes (for us these are $2 \times 2 \times 2$ and $2 \times 2 \times 4$, which involve 24 and 48 links, respectively). For larger volumes, the number of states requires serious numerical effort at the limit (or beyond) what is currently feasible on high-performance computing setups. Moreover, in higher dimensions, increasing the linear dimension by a unit amounts to increasing the total number of links proportional to the surface area.

To gain some insight into the physics despite these limitations, we construct a truncated Hilbert space (sometimes also called a limited functional space) starting from the energetically lowest-lying states and systematically introducing excitations to form new basis states [similar strategies have been applied in ED-like studies for various other physical systems see, e.g., [26,27]]. In the present case, the energetically most favorable states at large negative λ are the ones with the most flippable plaquettes. An excitation can then be introduced by flipping single plaquettes, which constructs a new state while respecting Gauss' law. Exhausting all maximally flippable states in this way, one obtains a set of states that differ by a single flip from the lowest-lying states, in the following denoted as "flip level" 1 (FL1). Higher FLs are reached by repeatedly applying this procedure to the newly found states. In fact, this is an alternative method to construct the full list of GLS. However, a tiny subset of nonflippable states are omitted in this way and this procedure

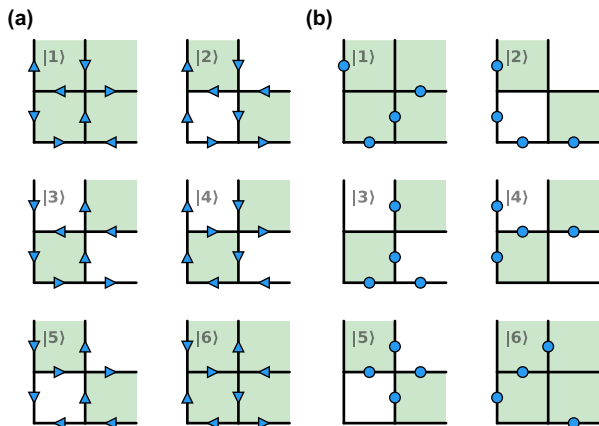


FIG. 4. Cartoon states of the zero-winding sector for a 2×2 lattice in the spin (a) and particle (b) representations. Green (white) shaded plaquettes are flippable (nonflippable).

may be stuck in disjoint pockets of the Hilbert space, which is sometimes called fragmentation of Hilbert space in the literature [28–30]. Nevertheless, as we will see, the unflippable states are not of interest for this study, and further no Hilbert-space fragmentation is present for the square-lattice Hamiltonian.

While it is obvious that eventually the spectrum of the truncated Hilbert space will converge to the true spectrum, we expect that the convergence sets in early such that we may extract useful information about the finite-size scaling of the mass gap. As it turns out, this approach is feasible and allows us to study the physics of the lattice $2 \times 2 \times 6$, having 72 links, without the need to fully diagonalize the entire Hamiltonian. Further details, including the convergence analysis for the $2 \times 2 \times 4$ system, are shown in Appendix B.

IV. DISTINGUISHING THE BOSONIC AND FERMIONIC QUANTUM LINK MODELS

The $U(1)$ quantum link model in $(2+1)D$ has been extensively studied on the square lattice in the spin- $\frac{1}{2}$ representation [14,31]. Therefore, we begin our investigation with the $(2+1)D$ fermionic model, attempting to understand if it has different properties from the one realized with quantum spins. We further examine the spin and fermionic versions of the model in $(3+1)D$ for similarities and differences.

A. Two dimensions

In order to understand the differences and the similarities between the fermionic and bosonic representations of the lattice gauge theory, we begin by considering the simplest possible setting: the case of the 2×2 lattice with periodic boundary conditions. For this system, there are four sites, and eight links. Implemented without any further constraints, the system would have $2^8 = 256$ states, but imposing Gauss’ law of $Q_x = G_x = 0$ for every site gives rise to only 18 total states of the system. Using the global winding-number symmetry, there are only six states in the zero-winding sector, in both the spin and the fermion representations as shown in Figs. 4(a) and 4(b), respectively.

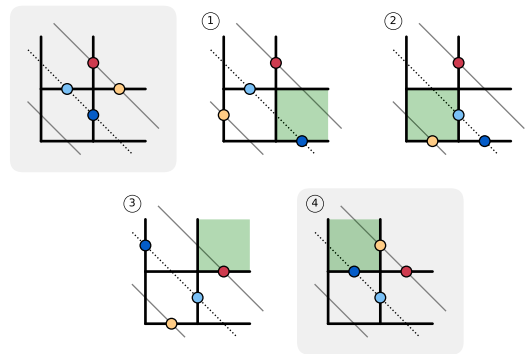


FIG. 5. Restricted movement on the 2D lattice. The nature of the plaquette interaction constrains the “paths” of the fermionic particles in two dimensions along diagonal tracks, illustrated by the lines in this particular 2×2 example. Effectively, the plaquette interaction causes two correlated simultaneous hops along two adjacent one-dimensional chains. In the numbered figures, the green highlighted plaquettes illustrate the particular Hamiltonian term being applied in each step. The only sign for the fermionic case that could occur is due to the boundary, but the fact that the particles move in pairs ends up precluding this possibility.

The action of the Hamiltonian for both the bosonic and fermionic models (when $\lambda = 0$) on the different states, as numbered in Fig. 4, is then given by

$$\begin{aligned}
 H|1\rangle &= -J(|2\rangle \pm |3\rangle + |4\rangle \pm |5\rangle), \\
 H|2\rangle &= -J(|1\rangle \pm |6\rangle), \\
 H|3\rangle &= -J(\pm|1\rangle + |6\rangle), \\
 H|4\rangle &= -J(|1\rangle \pm |6\rangle), \\
 H|5\rangle &= -J(\pm|1\rangle + |6\rangle), \\
 H|6\rangle &= -J(\pm|2\rangle + |3\rangle \pm |4\rangle + |5\rangle).
 \end{aligned} \tag{20}$$

(Details are given in Appendix C.) In the bosonic case the upper (positive) signs in Eq. (20) are taken, and in the fermionic case the lower (negative) signs are taken. The spectrum obtained in the two cases, however, is identical.

Naively, this seems surprising since from the analysis of spin and fermionic models one knows that in the latter, the fermionic world lines can exchange positions in two spatial dimensions, which gives rise to different physics as compared to the bosonic version. Therefore, it must be that the nature of the four-body interactions, necessary to preserve gauge invariance, also forbids all those paths which could otherwise differentiate between the hard-core bosons and the fermions. A geometric proof of this is provided in Fig. 5, which can be easily extended to any square (or rectangular lattice) with linear dimension L . Note, further, that the proof can be extended for all the superselection sectors labeled by different values of charges Q_x . We have explicitly repeated the exercise on the 2×2 lattice for all possible values of the fermion occupation (i.e., without imposing the Gauss law), and obtained an identical spectrum for both the spin links and the fermion links. This implies that the physics of the fermionic model is also the same as the ones already studied before.

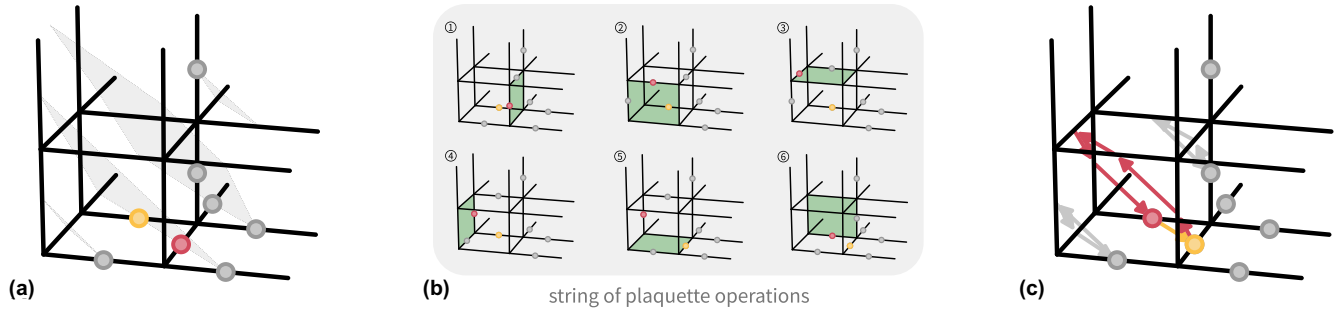


FIG. 6. Difference between bosonic and fermionic links. Starting from a given initial position on a $2 \times 2 \times 2$ lattice (a) one may follow a “path” of two fermions by successively applying suitable plaquette flipping operators (b, application from top left to bottom right). Finally, one ends up in the initial configuration with an effective interchange of two fermions (c), implying a sign that is not present in the bosonic model.

B. Three dimensions

In three spatial dimensions, we can extend the geometric proof outlined for two spatial dimensions. In this case, the particles are restricted to move on planes, and it is possible for a particle to make an orbit without disturbing any other particles in the plane. To see this, consider the example depicted in Fig. 6: Starting from an initial configuration [Fig. 6(a)], one may apply a string of plaquette operators that move the particles according to the paths shown in Fig. 6(b). In the final configuration [Fig. 6(c)], all links returned to their original occupation number with an effective interchange of the colored particles (the exact algebra for the applied operators is carried out in Appendix D). While in the bosonic case there is no sign associated with this exchange, the fermionic nature of the gauge particles requires a sign, therefore, the physics of both models is expected to exhibit distinct effects.

Thus, we obtain the very interesting result that interactions responsible for maintaining gauge invariance restrict world lines which cause particles to swap positions on the square lattice, thus rendering the statistics of the particles irrelevant. However, in three spatial dimensions, this is no longer the case, the particles move along planes, and the bosonic and the fermionic physics differ since the world lines which give different signs to the bosons and fermions can occur. Interestingly, the subdimensional motion of particles observed in this model due to the gauge interactions is reminiscent of fractonic physics [32].

V. PHYSICS IN THREE DIMENSIONS

In this section we numerically explore the physics of both the spin- $\frac{1}{2}$ bosonic and fermionic versions of the QLM in 3D, which we have shown to have distinct world-line weights to each other, in contrast to in 2D. Another difference compared to the 2D system is that in 3D there is no configuration on the lattice that allows all plaquettes to be flippable simultaneously, regardless of the statistics of the gauge particles. As we shall see below, this leads to a different broken symmetry in the ordered phase expected at a large negative RK coupling λ on 3D lattices as compared to 2D. We present results for several observables to explore both the bosonic and fermionic models, emphasizing the different features found in both cases.

A. Spectrum vs λ

As our first quantity of interest, we study the low-energy spectrum and its dependence on the RK coupling λ . In Fig. 7(a), the spectra for both bosonic (top) and fermionic (bottom) links are shown. First, we note the similarity of the low-energy spectra of both models at large negative λ , which persists up to $\lambda \lesssim -1.0$. This comes as no surprise since in the limit of $\lambda \rightarrow -\infty$ the particle statistics, i.e., the plaquette flipping term in the Hamiltonian, does not play any role and arguments may be made purely based on energetic considerations. Hence, in this limit the 3D system wants to maximize the number of flippable plaquettes. However, as mentioned above, not all plaquettes can be made flippable at the same time: only $\frac{2}{3}$ of the total number of plaquettes $N_p = 3 \times L_x \times L_y \times L_z$. The maximally flippable configurations are achieved by stacking fully flippable layers in a given planar direction while maximizing the number of flippable plaquettes along the remaining two planar directions. For a given direction, this stacking while retaining the maximal number of flippable plaquettes can be done in four ways, such that in total there are 4×3 most flippable configurations which correspond to the “half-filled” or particle-hole symmetric case (in the spin picture this would be $S_z = 0$). Therefore, at $\lambda \rightarrow -\infty$ we observe a 12-fold degeneracy in the spectrum. It turns out that these states are related via the transformation of the group $D_{3h} = D_3 \otimes \mathbb{Z}_2$, which represents the direct product of the lattice rotation in 3D and the charge conjugation, respectively. All states belonging to this multiplet are expected to be degenerate in the thermodynamic limit (TL), and therefore this symmetry is spontaneously broken in this phase.

This observation is further elucidated in Fig. 8(b), where the volume scaling of the lowest few energy gaps in the bosonic model is shown for a reference value of $\lambda = -3.0$, which is deep in the symmetry-broken phase. The spectrum for the fermionic model is virtually indistinguishable from the bosonic model in that regime, and so the low-energy spectra for both models differ by less than 1%. As expected from the above arguments, the lowest 11 gaps decay exponentially while higher-lying energy values decay more slowly, seemingly polynomially. Moreover, the inset of the same figure shows the lowest 12 states for a $2 \times 2 \times 2$ lattice, revealing a structure with six energy manifolds consisting

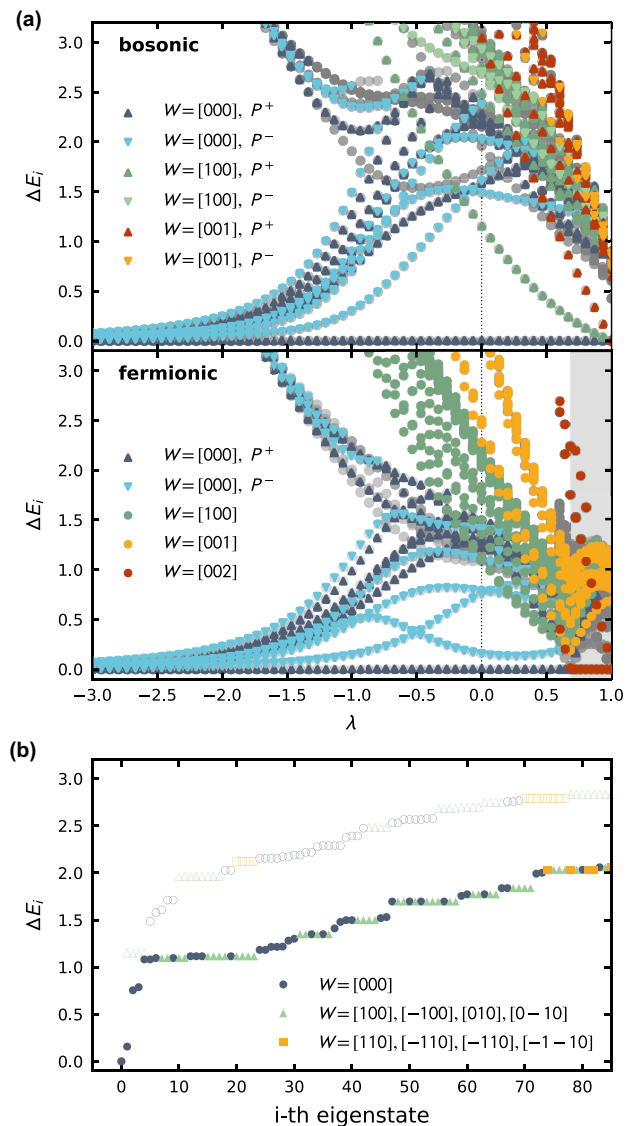


FIG. 7. Low-energy spectrum for $2 \times 2 \times 4$ lattices with bosonic (a, top panel) and fermionic (a, bottom panel) links. For fermions, the gray shaded area marks the region where the ground state is in the nonzero-winding sector. (b) Lower part of the spectrum for bosons (open symbols) and fermions (solid symbols) at $\lambda = 0$, corresponding to the dotted vertical lines in (a).

of $1 + 2 + 3 + 3 + 2 + 1$ states. This corresponds exactly to the dimensionality of the irreducible representations of the D_{3h} group, where the (numerically) exact degeneracies are a consequence of the non-Abelian nature of this group.

At larger values of λ , the competition between maximizing flippability and the kinetic term in Eq. (8) may potentially lead to a phase transition out of the ordered phase. Earlier studies of dimer models (with bosonic links) on other 3D lattice geometries [18,19] suggested the emergence of a quantum spin-liquid (QSL) phase that persists at intermediate λ values up to the RK point at $\lambda = 1.0$. A study of hard-core bosons on the pyrochlore lattice, which gives rise to the QLM (also on the pyrochlore) in the low-energy limit, was also shown to have a QSL phase [17]. One of the hallmarks of

such QSLs is the absence of any sort of symmetry breaking in the ground state in the thermodynamic limit, which in itself is challenging to establish rigorously. A sense of this can already be obtained from Fig. 7(b), which shows the low-energy spectra of both the bosonic and the fermionic QLMs in different winding sectors. We note the presence of a large number of low-lying energy eigenstates above the ground state for both the cases, without the presence of any large gap. This indicates the possibility of smooth excitations which have overlaps with the low-lying eigenstates, and consequently a smooth spectral function lacking any distinctive energy scale, which is typical of a liquid phase. This is in sharp contrast to the nematically ordered phase, where above the manifold of 12 states there is a large window which hosts no energy eigenstates. Consequently, excitations there are peaked around a certain frequency and typical of a symmetry-broken solid phase. We have noted that this distinction between the two regimes persists for our system sizes, and therefore if the trend continues to the TL, a liquid phase with continuous excitations is reasonable in the $\lambda \sim 0$ region.

Moreover, one may investigate the volume scaling of the gap between the ground and the first excited states, where the absence of any exponential decay of the gap, ΔE_0 , would be indicative of such a liquid phase around $\lambda \sim 0$. In Fig. 8(a), we show results for the lowest-energy gap for bosonic link variables for two representative values of λ . The left panel at $\lambda = -3.0$ again reflects the symmetry-broken phase [cf. Fig. 8(b)] where the gap to the first excited state decays exponentially with the volume, as one would expect for a symmetry-broken phase. Conversely, the right-hand panel of the same figure corresponds to $\lambda = 0$ and displays a much slower decay. Moreover, we note that in the $\lambda = 0$ phase, the lowest excitation is a winding string in the shorter directions [100] and [010], while the lowest excitation within the zero-winding sector costs more energy. This is an interesting indication that the vacuum is stable to the creation of strings, another signal for a possible Coulomb phase. The values of λ were chosen solely to be representative of the respective regimes, and their numerical values do not correspond to quantitatively important aspects of the phase transition. The data points for the largest system, here $2 \times 2 \times 6$, have been obtained with the low-energy approximation discussed above and are in agreement with this trend.

While this analysis presents some evidence for a transition between an ordered phase and a potential QSL, the obtainable lattice sizes limit our ability to make definitive statements. Moreover, the exact transition point (if present at all) is impossible to pinpoint with ED with the few lattice sizes that we possess. A natural next step would be to address these issues by means of *ab initio* calculations, such as a Markov chain Monte Carlo. However, for the fermionic model, sign problems currently preclude the existence of any efficient Monte Carlo algorithm to our knowledge, and different numerical approaches such as tensor network methods [33–35] might be necessary.

While the volume scaling of the gap is here only presented for bosonic link variables, we observe qualitatively similar behavior for fermionic links and therefore expect the transition between an ordered phase and a QSL for both models (we return to this point in Sec. VC). However, despite the simi-

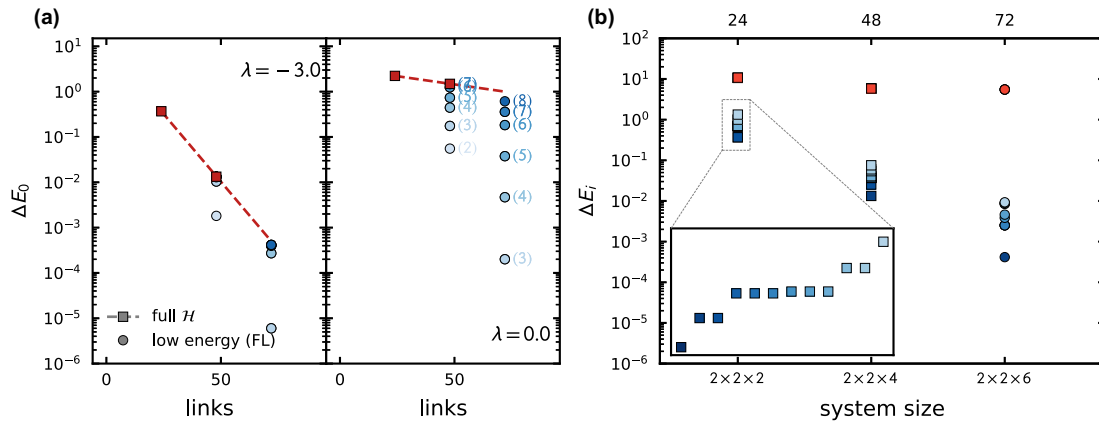


FIG. 8. Finite-volume behavior of the low-energy spectrum for bosonic links. (a) Finite-size scaling of the gap to the first excited state on a y -log scale. Fast decay for $\lambda = -3.0$ (left panel) versus a slower decay for $\lambda = 0$ (right panel). (b) Gaps to the lowest 11 excited states are shown in blue shades, higher excited states in red. The scale on the top denotes the corresponding number of links. (Inset) Degeneracy structure of the ground-state manifold on a $2 \times 2 \times 2$ lattice. In all panels, squares denote results from a diagonalization of the full Hilbert space \mathcal{H} , whereas circles show low-energy results from a reduced Hilbert space with the level of approximation indicated in parentheses (see main text). Dashed lines are a guide to the eye.

larities of the low-energy spectrum in both models, there are two important differences. The first observation concerns the winding numbers of the first excited state in the potential QSL phase, which seem to be nonzero only for the bosonic case. The model with fermionic degrees of freedom has another state of the zero-winding sector as first excited state (although with different parity as the GS). Only upon increasing λ further do we observe the eigenstates with nonzero-winding approaching the ground state.

Interestingly, there is a second key difference between the models in that the fermionic model even features a ground-state level crossing at $\lambda_{c_2} \approx 0.65$ for the lattice $2 \times 2 \times 4$, which is absent for the bosonic links. Beyond this λ_{c_2} , and up to the RK point, the GS is in the $W_x = W_y = 0$ and $W_z = 2$ winding sector, indicated by the gray-shaded area in Fig. 7(a). Therefore, the system seems to enter a “flux-condensed” phase where it is energetically advantageous for the system to have flux lines along the long direction of the tubelike lattice. It will be interesting to see whether this feature persists in the TL.

B. Ground-state fidelity susceptibility

In order to further shed light on whether the explored parameter range of λ crosses a phase transition, one can also exploit tools from quantum information theory. Specifically, in this section we present results for the ground-state fidelity, which measures the overlap between two ground states with a slight difference in the coupling. The overlap exhibits a dip if the two corresponding ground-state (GS) wave functions are qualitatively different, i.e., when the states belong to different quantum phases, and hence is a useful witness to detect quantum phase transitions [36]. Here, we are interested in the GS fidelity as a function of λ , defined as

$$F(\lambda, \epsilon) = |\langle \psi(\lambda) | \psi(\lambda + \epsilon) \rangle|, \quad (21)$$

where ϵ denotes the difference between the two involved λ values. Note that the fidelity itself depends on ϵ since, naively,

the overlap between two “neighboring” states increases when the parameter offset is reduced (since the states are “closer”). Moreover, this overlap is expected to vanish exponentially with increasing system size, in accordance to predictions of random matrix theory [37]. To overcome these shortcomings, it is more convenient to introduce the fidelity susceptibility formally defined via

$$\chi_F \equiv - \left. \frac{\partial^2 \log F}{\partial \epsilon^2} \right|_{\epsilon=0}. \quad (22)$$

Much like thermodynamic susceptibilities [38], the fidelity susceptibility encodes the response of the GS overlap to a small change in the driving parameter λ . Moreover, just like the fidelity of order parameters, the positions of the maxima in χ_F at finite-system sizes can be used to extract critical properties for infinite systems via finite-size scaling [38,39].

Computationally, there are several ways to extract the fidelity susceptibility (see, e.g., Ref. [39] for an overview). A straightforward way is to simply take the overlap according to Eq. (21) and then exploit the relation

$$F(\lambda, \epsilon) = 1 + \frac{\epsilon^2}{2} \chi_F(\lambda) + O(\epsilon^4), \quad (23)$$

which may be obtained via first-order perturbation theory [38,40]. A potential drawback is a systematic error induced by the finite difference ϵ , however, this can be efficiently suppressed by using small enough ϵ .

In Fig. 9 we show results for the fidelity susceptibility on both lattice sizes studied in this work for bosons (top) and fermions (bottom). For the bosonic link model we observe a peak for $\lambda \sim -1$, hinting at the presence of a smooth phase transition, and thereby suggesting that for λ close to zero, the system probably comes out of the ordered phase. At positive λ the susceptibility dips before a steep increase heralds the presence of the RK point at $\lambda = 1$ (which separates a potential QSL from a staggered dimerized ground state with no flip-plaquettes). Close to the RK point, the ground state is

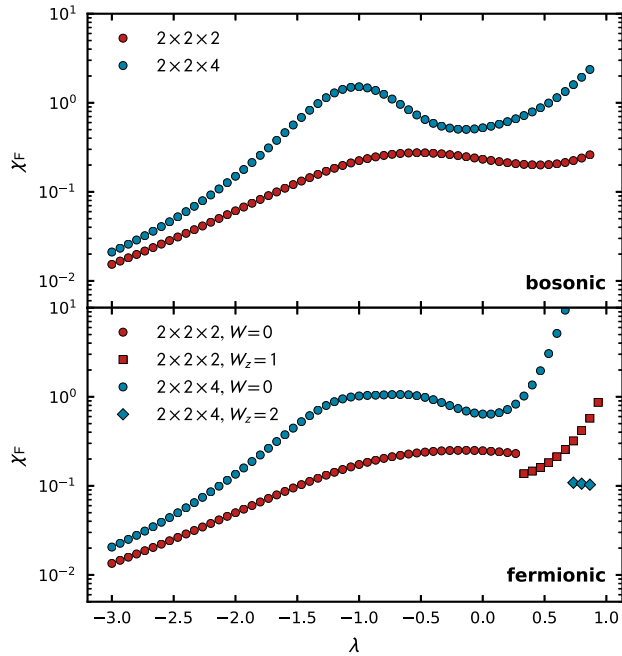


FIG. 9. Ground-state fidelity susceptibility for two system sizes for bosonic (top) and fermionic (bottom) links. Note the log-scale on the y-axis.

sensitive to states with winding strings, and this shows up as a sharp increase in χ_F .

For the case of fermionic links, the overall behavior is similar; however, a qualitative difference arises: while the sharp rise in the vicinity of the RK point as well as the smooth peak at $\lambda \sim -1$ are present as in the bosonic case, the curves for both shown system sizes exhibit a discontinuity. Unsurprisingly, this jump occurs at the point where we observe the ground-state level crossing in the spectrum, i.e., where a potential first-order transition takes place. For both lines shown in the lower panel of Fig. 9, the solid circles are the values in the zero-winding sector whereas the filled squares reflect the susceptibility in a nonzero-winding sector, which hosts the ground state in this regime.

Based on these findings and the discussion in the previous section, we propose the qualitative phase diagram on the λ axis shown in Fig. 1. For both the bosonic and fermionic link models, there seems to be a smooth quantum phase transition at moderately negative λ . Additionally, for fermionic links a sharp transition to an as-of-yet unknown phase seems to exist, however, it is challenging to predict if this persists in the thermodynamic limit. In the next section, we investigate other observables to establish some properties of the putative quantum phases.

C. State participation and entropy

In order to further characterize the ground-state behavior, we investigate the structure of the ground-state wave function at representative values of the RK coupling λ in the different phases. As a first step, we discuss a correlation histogram that relates the number of flippable plaquettes for a given basis state with the relative weight of this basis state in the GS wave

function on a $2 \times 2 \times 4$ lattice, shown in Fig. 10 for both the bosonic and the fermionic links.

While both scenarios look fairly similar, let us first discuss the case of bosonic links (left column). At a representative value for the rotational symmetry-broken ordered phase, for which we take $\lambda = -3.0$, the ground-state wave function $|\text{GS}_{\lambda=-3.0}\rangle$ is in the $W = [000]$ sector (red symbols). Both Figs. 10(a) and 10(b) show the absolute value of the overlap of the i th basis state with the ground-state wave function: $c_i = \langle i | \text{GS} \rangle$. The y axis of Fig. 10(a) shows the number of basis states which have the same overlap with the wave function, while Fig. 10(b) shows the total number of flippable plaquettes for the corresponding basis states. As is apparent from Fig. 10(b), almost the entire weight in this regime is carried by basis states with the largest number of flippable plaquettes. This is indicated by the isolated scatter points in the top right corner. Indeed, this is not unexpected since we already argued above that in this phase the D_{3h} -symmetric states constitute the GS manifold at $\lambda \rightarrow -\infty$. The relative importance of these few states becomes even more apparent by considering the corresponding histogram of the weights of the GS wave function (not resolved in the number of flippable plaquettes), shown of Fig. 10(a). Here, the isolated point corresponds to the single peak with the largest weight and all the other basis states contribute with weights smaller by several orders of magnitude (note the logarithmic scale).

At larger values of λ , we have argued based on the scaling of the energy gap to the first excited state that symmetry breaking might be absent, and the system enters a disordered QSL phase. Performing an equivalent analysis on the representative wave function at $\lambda = 0.0$ (blue data) indeed reveals a picture consistent with the conjecture of a liquid phase: The amplitude in $|\text{GS}_{\lambda=0.0}\rangle$ is carried by many states with vastly different number of flippable plaquettes, all with similar amplitudes. This is reflected by the relatively flat distribution in Fig. 10(b) and by the narrow histogram in Fig. 10(a). Moreover, the distribution of the weights is localized around the value for an equal superposition of all states in the $W = [000]$ winding sector, indicated by the vertically dashed line. The deviation from this ideal result could become smaller with increase in the lattice size.

Let us turn to the case of fermionic links, which is shown in the right panel of Figs. 10(c) and 10(d), which plot the same physical quantities as those in Figs. 10(a) and 10(b), but for the fermionic model. For values of λ up to the ground-state level crossing at $\lambda_{c2} \approx 0.65$, the overall picture of the correlation histogram is very similar to the bosonic case since the GS also is in the zero-winding sector. However, in contrast to the bosonic case, many more states have zero weight (within machine precision). This could be due to some unresolved symmetry for the fermionic model causing the coefficients of basis states with the same number of flippable plaquettes to be equal and opposite, which then conspire to cancel out. A striking difference between the bosonic and the fermionic links occurs only above λ_{c2} , when the ground state is in the $W = [002]$ sector. We show the corresponding analysis of representative state at $\lambda = 0.8$ (green data) and it immediately becomes apparent that most lattice configurations again have very small weights. Conversely, the states with nonzero weight are observed to contribute equally to a very

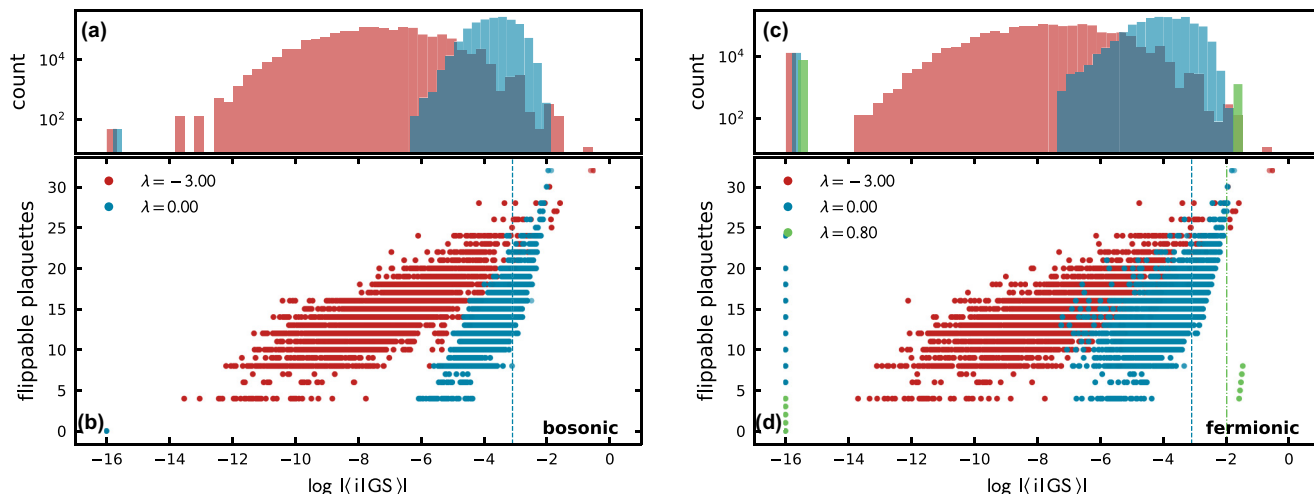


FIG. 10. Correlations between the weight and the number of flippable plaquettes of basis states in the ground state for bosonic (left) and fermionic (right) links on a $2 \times 2 \times 4$ lattice. (Top row) Histogram of the logarithm values of the absolute value of the weight. At large negative $\lambda = -3.0$ only a few states contribute significantly, while others have significantly reduced weight and are spread over orders of magnitude. At $\lambda = 0$ the distribution is narrow, corresponding to a more even distribution of weight among the states. (Bottom row) The number of flippable plaquettes vs the logarithm of the absolute value of the amplitude. The dashed line marks an even superposition of all states.

good approximation. This phase therefore is indicative of an ordered phase which happens close to the RK point in the fermionic model. For orientation, the green dashed-dotted line shows the corresponding amplitude of an equal superposition of all states in the $W = [002]$ sector, and we see that all the contributing states are to the right of this line.

The visual investigation of the structure of the GS wave function above, which suggests the delocalized nature of the wave function in the Hilbert space in the potential spin-liquid phase, could also be made more concrete with other observables typically used to diagnose delocalization in Hilbert space [41]. Specifically, we discuss the Shannon entropy, which can be written as a special case S_1 of the Rényi entropy of order α :

$$S_\alpha = \frac{1}{1-\alpha} \log \sum_{i=1}^N p_i^\alpha \stackrel{\alpha \rightarrow 1}{=} - \sum_{i=1}^N p_i \log p_i, \quad (24)$$

where the probability $p_i = |\langle i | \text{GS} \rangle|^2$ is the weight of the basis state i in the ground state. Note that such entropies are dependent on the chosen many-body basis, but the values are not expected to be very different as long as the basis is not fine tuned. The intuition behind this observable is a quantification of the amount of fluctuations in the ground-state wave function: While a maximally localized ground state would correspond to minimal values of S_1 , the entropy grows with the amount of fluctuation to its maximal value when all states contribute equally (when it is maximally disordered).

In the top panels of Fig. 11, we show our numerical values of S_1 for bosonic (left) and fermionic (right) link models for two system sizes. In both cases, the ordered limit at $\lambda \rightarrow -\infty$ would correspond to $S_1 = \log(12)$, which is indicated by a black dashed line. We observe that S_1 for both system sizes converge to this limit. In the opposite limit, namely $\lambda \rightarrow 1$, we observe that the Shannon entropy for the bosonic link

model quickly approaches the maximal value $S_1 = \log N_W$ where $N_W = |\mathcal{H}_W|$ denotes the size of the Hilbert space in the corresponding winding sector. This supports the picture from the above analysis, namely, that the system exits the ordered phase as λ is made small and positive, and enters a QSL phase which smoothly merges to the RK point $\lambda = 1$.

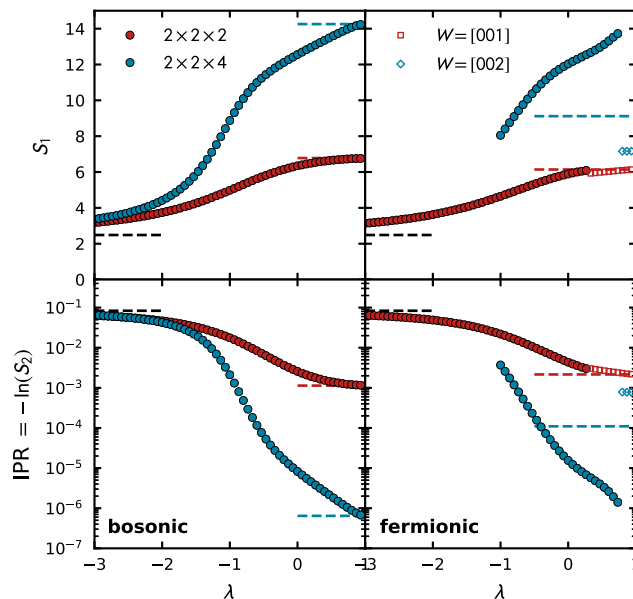


FIG. 11. Entropy and IPR vs λ for bosonic (left) and fermionic (right) link variables are shown in the top and bottom lines, respectively. The respective limits are shown with dashed lines. For all plots, full symbols correspond to zero-winding states whereas open symbols (for fermions) correspond to non-zero-winding sectors, as indicated in the legend.

For fermions a slightly different picture presents itself, which depends on the considered lattice size. While similar features to the bosonic case persist, above λ_{c2} the entropy is expected to converge to $\log N_{00z}$, which is indicated by the colored dashed lines. This is indeed the case for the $2 \times 2 \times 2$ lattice (for the $W_z = 1$ sector), where all states contribute almost equally irrespective of the λ value. For the larger $2 \times 2 \times 4$ lattice, S_1 settles at a smaller value, indicating that the ground state of the system now resides in a reduced number of states in the $W = [002]$ sector. This is completely consistent with the above analysis where the GS histograms in the same region showed that the weight of any state either vanishes or is approximately equal to all other nonzero weights.

For completeness, we also briefly discuss here a closely related quantity, namely, the so-called inverse participation ratio (IPR) [41], defined via

$$I = \sum_{i=1}^N p_i^2. \quad (25)$$

The IPR is an alternate probe for localization of a quantum state in a given many-body basis and is related to the Rényi entropy of order $\alpha = 2$ via $S_2 = -\log I$ such that both I and S_1 encode similar information. We show our numerical values for the IPR in the lower panels of Fig. 11, where we can draw equivalent conclusions as for the entropy discussed above: While the ground-state wave function is dominated by the 12 most flippable states at large negative λ (convergence to the black dashed line at $I = \frac{1}{12}$ irrespective of the system size) the IPR approaches the one of an equal superposition of all basis states in the given winding sector (appropriately colored dashed lines at $I = 1/N$) and is, hence, reminiscent of a QSL-type behavior.

D. Monopole string excitation

One way to characterize the putative U(1) liquid phase at λ values close below the RK point is to investigate the cost of the flux lines in the system. The emergence of these flux lines is illustrated in Fig. 12(a): Starting from a state in the zero-winding sector (top left panel), where $G_x|\psi\rangle = 0$ on all vertices, we flip an arbitrary link E_x, μ . Such a configuration is not in the pure-gauge sector, as Gauss' law at x and $x + \hat{\mu}$ now corresponds to a positive and a negative charge sitting at these vertices, respectively. The flipped link acts as a “flux line” between these opposite charges (marked as the red arrows in the figure). Further, separating these charges prolongs these flux lines, until eventually the charges cross the boundary and annihilate each other leaving behind a line of flipped links with the condition $G_x|\psi\rangle = 0$ is again fulfilled at every vertex. As opposed to the initial basis state, the resulting state acquires a nonzero-winding number and therefore does not belong to the zero-winding sector.

In a confined phase, it is energetically costly to separate the charges, and the energy cost scales linearly with the distance between the pair of charges. The strength of this confinement is determined by the constant of proportionality, commonly referred to as the string tension σ , defined via $V(R) = \sigma R$ where $V(R)$ is the potential between two opposite charges.

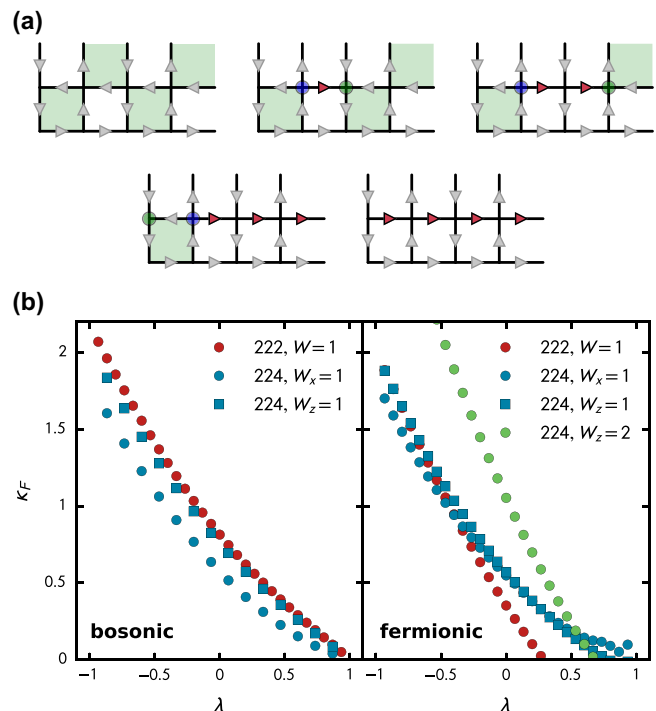


FIG. 12. Monopole string excitation. (a) Sketch of the emergence of a flux line. (b) κ_F for two system sizes as a function of λ for bosonic (left) and fermionic (right) links. For the tubelike lattices, we plot two lines: one for fluxes along the short (disks) direction and one for the long (squares) direction.

In a deconfined phase, as is expected in a U(1) liquid phase, these “flux excitations” should cost much less energy, i.e., the string tension should be small. Of course, at finite system size this behavior is challenging to address precisely, however, the flux excitations should be cheaper for $\lambda_c \geq \lambda \geq -1$ (where we expect such a phase) than for the ordered state at large negative λ .

Following [19], we investigate the cost of such a flux-line excitation by measuring the monopole string tension, defined as

$$\kappa_F = \frac{E_F - E_0}{L_F} = \frac{\Delta_f}{L_f}, \quad (26)$$

where E_F is the ground-state energy in the lowest nonzero-flux sector, E_0 is the ground state in the zero-flux sector, and L_F denotes the length of the flux tube [corresponding to the difference between the last and first panels of Fig. 12(a), divided by the length of the flux line].

Results for this quantity are shown in Fig. 12(b) for the two system sizes reachable with ED. For the bosonic case (left panel) we indeed observe the aforementioned trend, with a slight tendency to move towards the expected results for the thermodynamic limit (which is well beyond ED studies). There, κ_F should only be nonzero for $\lambda < \lambda_c$ but vanish above in the U(1) liquid phase. Although the authors of Refs. [18,19] study the related dimer model (which has the identical Hamiltonian, but a different superselection sector) we find qualitatively similar results for the monopole string tension for the small systems studied here.

For the fermionic case, on the other hand, the picture is slightly more complicated. There, the ground-state level crossing between the zero- and nonzero-winding sectors implies a vanishing cost of excitations for flux lines of arbitrary length. This is apparent in the right plot in Fig. 12(b) where κ_F crosses over to negative values. We interpret this as a flux-condensed phase beginning, at least for the finite sizes considered here, already below the RK point. As the crossing point shifts to higher values of λ with increasing system size, it will be interesting to see whether such a phase can be stabilized in the TL. While this implies that the RK point does not have its usual properties for the finite-size fermionic system, we expect the properties to be restored in the thermodynamic limit. In particular, we would expect the GS to have an equal superposition of basis states from all the different winding sectors for larger system sizes.

VI. CONCLUSIONS AND OUTLOOK

In this paper, we have introduced the particle representation for the Abelian $U(1)$ QLMs, distinct from the rishon representations considered before [8]. We noted that while the physics of using hard-core bosons (which are equivalent to using quantum spins) to represent the link operators give identical physics as that of using fermions in two spatial dimensions, the physics is qualitatively different in three spatial dimensions. Interpreting the plaquette term as a correlated hop of *two* fermionic particles along two adjacent links diagonally intersecting the midpoint of perpendicularly oriented links, as shown in Fig. 3, we could show that these particles have subdimensional motion under the kinetic term. For two spatial dimensions, this implied a linear motion of the particles, and any negative signs due to fermions crossing the periodic boundary gets canceled by the hop of the paired fermion. In three spatial dimensions, the fermions move along a plane in two spatial dimensions and give rise to an opposite sign to a world line as a boson. Therefore, the fermionic operators give rise to different physics as the bosons in three and higher dimensions.

Using techniques of finite-size scaling on results obtained from lattices up to 72 links, we showed that both the fermionic and the bosonic models spontaneously broke the lattice rotation and the charge-conjugation symmetry for large and negative λ . On decreasing λ towards zero, our results indicated that the symmetry-breaking gap dissolves and the gap does not decrease. We introduced the state-participation histogram as a tool to identify any sign of symmetry breaking in the ground-state wave function. This diagnostic clearly indicates the absence of any special basis state in the region $\lambda \sim 0$ with any significant overlap with the ground-state wave function. In addition, a host of other observables such as the mass gap, the fidelity susceptibility, as well as several related information theoretic quantities reveal the absence of any symmetry-broken phase, and provide an indirect evidence of a $U(1)$ Coulomb phase, which is sometimes identified as a spin-liquid phase in the condensed matter theory literature. Both the fermionic and the bosonic models show these features, even though the potential liquid phase is possibly very different in the models. For example, the winding strings are

much easier to excite in the regions $\lambda \sim 0$ of the bosonic model, as compared to the fermionic model.

Of course, the existence of this liquid phase is fascinating and needs to be investigated on larger lattices. One could marginally extend our calculation by exploiting various commuting symmetries to reach larger system sizes using exact diagonalization. However, this is likely going to be insufficient, and some stochastic Monte Carlo methods, or tensor network methods, would be more useful to achieve significant progress here.

For the fermionic model, we observe a phase which is sandwiched between the liquid phase and the RK point. This phase has condensed phases in the ground state, and is reminiscent of the staggered phase (which is stable for $\lambda > 1$ in both the models in two spatial dimensions). However, the ground state has winding strings only in the longer direction and none along the shorter direction. This could be a finite-size effect, disappearing in the thermodynamic limit to the usual RK point where the ground state is spread over all the winding sectors.

With the rapid advance in the field of quantum simulators using cold atoms or with Rydberg atoms, it is natural to imagine that such platforms can be used to realize the model proposed here. Such an experimental realization would not only enable an independent verification of the physics proposed here, but also enable the study of quantum dynamics in this model which could possibly be beyond the reach of any numerical method in the near future. However, the three spatial dimensions involved in the problem provide a difficult challenge given the well-known difficulty of implementing the plaquette interaction in a cold-atom simulator [42]. However, we note that the possibility of realizing the plaquette interaction as a correlated hop could be an altogether practical route to realize the four-body interaction without the need of any auxiliary qubits as in a digital simulation scheme [43]. In this regard, our interpretation of the plaquette term as a correlated hop of particles could already extend the schemes provided in [44], which, however, was postulated for the limit of large boson occupation numbers. In fact, Ref. [45] already describes a Rydberg atom implementation of the fermionic t - V model which allows the fermions to hop along only one spatial direction. With additional interactions to force fermions in adjacent chains to hop together, one could realize exactly the plaquette interaction.

Independently of the experimental realization, this class of models opens up some interesting avenues of research purely from a quantum field theory perspective. One of the immediate questions is to ask if the Coulomb phase does indeed exist in the bosonic model in three spatial dimensions, is it possible to use dimensional reduction to obtain a confined continuum gauge theory in two spatial dimensions, which the so-called D-theory approach advocates [46]. Other interesting questions include the formulation of the field theory of a Coulomb phase in three spatial dimensions, where the gauge fields are fermionic in nature, the mechanism of including larger representations using fermionic states, as well as non-Abelian generalizations of the fermionic links. The presence of possible critical points and the phase diagrams in such models, together with synergies with experiments, promise an exciting road ahead.

ACKNOWLEDGMENTS

We acknowledge fruitful discussions with A. Sen, I. Sodemann, J. Steinegger, S. Chandrasekharan, and U.-J. Wiese. L.R. is supported by FP7/ERC Consolidator Grant QSIMCORR, No. 771891, and the DFG under Germany's Excellence Strategy – EXC–2111–390814868. Research of E.H. at the Perimeter Institute is supported in part by the Government of Canada through the Department of Innovation, Science and Economic Development and by the Province of Ontario through the Ministry of Colleges and Universities.

APPENDIX A: CONSTRUCTING THE GLS

The first step of the diagonalization routine consists of building the many-body Hilbert space of permissible states (i.e., those that fulfill the Gauss law on every vertex). A naive approach, i.e., listing all states and simply discard the ones that violate the constraint, is not useful because of the prohibitive scaling of the number of states. Here we offer two options how to efficiently construct the Hilbert space.

Recursive state search I. One way to construct all permissible states for bipartite lattices is to first divide the problem into the two sublattices. We call the sublattice Λ_A the one where we place vertices that obey Gauss' law (see main text) and the sublattice Λ_B which contains the “in-between” vertices where we need to check for the validity of Gauss' law. Then, one can proceed with a recursive function as follows:

(1) The (recursive) function should take in a list as its argument.

(2) If the list is of the length of the sublattice Λ_A , return the current list. The recursion is done and we have obtained a valid state.

(3) If the length of the list is shorter, then loop through all allowed vertices by Gauss' law:

(1) Append the current vertex to the original list.

(2) With the updated list, check which vertices of Λ_B are already surrounded by vertices on Λ_A . If there are surrounded vertices in Λ_B , check if Gauss' law is satisfied on this vertex. If not, terminate the recursion for this branch and return nothing; Gauss' law is violated and hence the state is not valid. If Gauss' law is satisfied, or if there are not surrounded vertices in Λ_B , call the recursion with the updated list.

Calling the function with an initially empty list creates a tree which is checked for validity on the fly. Only when the desired depth is reached (i.e., the size of the sublattice A) a state will be added to the list in the end. Therefore, once the recursion is finished, only the valid GLS survive.

Note that technically this could be problematic because for large systems this could lead to steep memory requirements. It is advisable to store the already obtained states to file at intermediate steps (buffered, for every 10^6 states for instance), in order to keep the list short.

Recursive state search II. The allowed GLS can also be found by a nested application of the “kinetic” part of the Hamiltonian to a set of seed states (the plaquette flipping term). This is efficient, but needs at least one flippable basis state for each winding sector in order to be useful. Moreover,

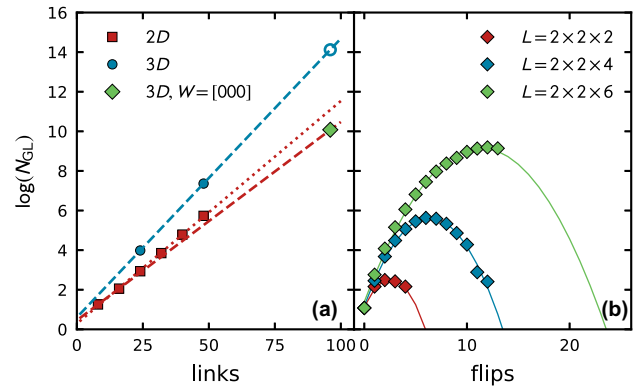


FIG. 13. Scaling of the number of GLS. (a) Total number of GLS, N_{GL} , for 2D (red) and 3D (blue) lattices, irrespective of winding. The dashed lines are an extrapolation with only the lowest data points, the dotted line uses all available 2D data points. The green diamond is an estimate for the size of the $W = [000]$ sector on a $2 \times 2 \times 6$ lattice. (b) Number of GLS in the $W = [000]$ sector as function of the flip level. Solid lines represent a quadratic fit.

there are two potential caveats: (1) unflippable configurations cannot be reached (which likely is not an issue except at the RK point) and (2) this strategy relies on the ergodicity of the problem. It could be, for instance, that the Hilbert space does fragment into several subspaces due to some hidden symmetry. Then, this strategy will in general not find all relevant states (see also [19]).

For completeness, we show the scaling of the total number of GLS for 2D and 3D lattices (across all winding sectors) in Fig. 13(a), where exact values are represented by filled symbols and (linear) extrapolations on the logarithm scale are shown as dashed and dotted lines. Clearly, the requirements for a $2 \times 2 \times 6$ lattice are steep, and it is likely that only the zero-winding sector of this lattice size could potentially be reached with ED (green diamond), which is still of the order of $\sim 2^{33}$ states (without the consideration of further symmetries, e.g., translational invariance).

APPENDIX B: CONVERGENCE OF LOW-ENERGY APPROXIMATION

As briefly discussed in the main text, we employ a systematic low-energy approximation for the largest considered systems in order to avoid the prohibitive scaling of the computational effort, allowing us to gain some information on systems larger than $V = 2 \times 2 \times 4$. Here we present some details of this approach.

The general idea is to first consider the ground-state manifold in the limit $\lambda \rightarrow -\infty$, which is a set of superpositions of the most flippable lattice configurations. In this limit, the lowest 12 states (this is the size of the GS manifold) could be extracted exactly by only considering the most flippable lattices. To systematically improve the obtained energies at $\lambda > -\infty$ we simply introduce “excitations” to the system by flipping single plaquettes. The extended set of states is expected to improve the approximation, as we now couple the low-lying states to excited states. Systematically repeating this sequence allows us to study the spectrum at different “flip

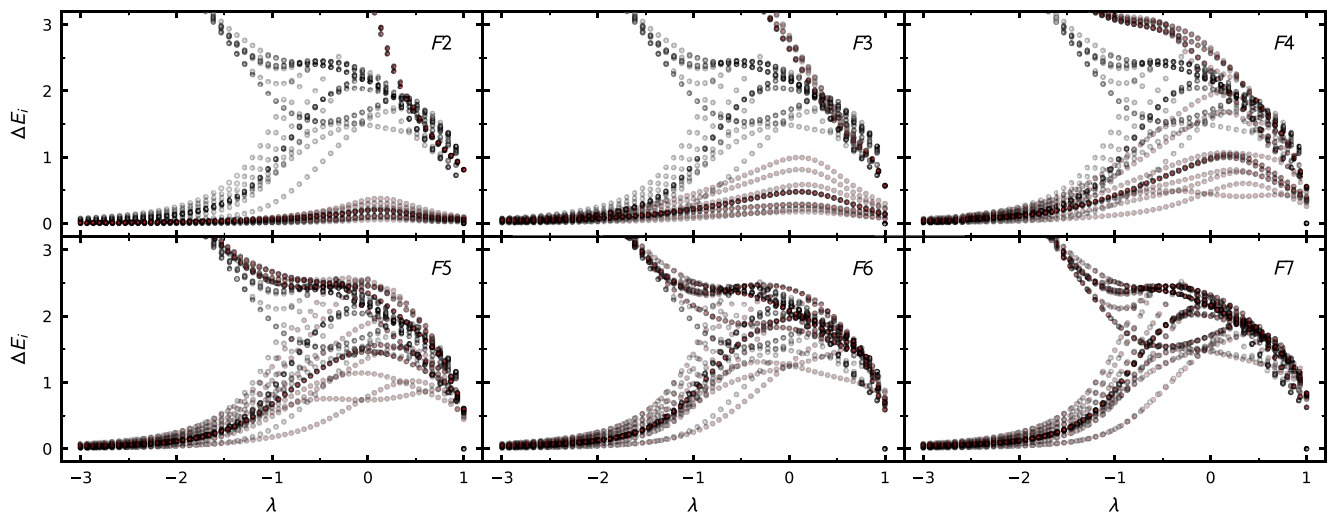


FIG. 14. Low-energy spectrum of a bosonic $2 \times 2 \times 4$ system with all states in the zero-flux sector considered (gray symbols) and with a restricted Hilbert space constructed from plaquette flips (red symbols). From top left to bottom right: 2, 3, 4, 5, 6, and 7 flips away from the maximally flippable manifold, respectively. Darker coloring indicates degeneracy.

levels” (FL); this is shown in Fig. 14 for a $2 \times 2 \times 4$ involving FL2 to FL7. At large negative λ , the spectrum converges quickly since only small corrections are expected to be of importance in this regime. In the region $\lambda \approx 0$ convergence sets in only at larger FL, indicating the importance of states with an arbitrary number of flip excitations. Clearly, at $\lambda = 1.0$ due to the massive degeneracy of states with finite-flux content at the RK point, higher flip levels will be needed to establish convergence of the spectra.

The values for the excitation energies within such an approximation at $\lambda = -3.0$ and 0.0 are shown in Fig. 7(b) and are observed to give a satisfactory convergence even at lattices with 72 link variables. For quantities other than energy gaps, however, convergence was observed to be more challenging.

Finally, we show the scaling of the number of GLS as a function of the flip level in Fig. 13(b) for different lattice sizes, and we also explicitly give the number and fraction of the total Hilbert space for a $2 \times 2 \times 4$ lattice in Table I.

TABLE I. Number of states for the respective low-energy approximations of the $2 \times 2 \times 4$ lattice in the [000] winding sector compared to the full number of states (last line).

FL	Number of states	%
0	12	0.00077%
1	396	0.0255%
2	5132	0.3307%
3	35660	2.298%
4	151864	9.785%
5	436088	28.1%
6	860664	55.45%
7	1245688	80.26%
All	1552024	100%

APPENDIX C: DIAGONALIZING THE 2×2 FERMIONIC AND BOSONIC CASES

In this Appendix, we explicitly work out the eigenvalues and the eigenvectors of 2×2 bosonic and fermionic systems, explicitly showing where they differ in negative signs. Before constructing the Hamiltonian explicitly for the 2×2 system, we can further simplify the analysis and the numerics by dividing the basis states into different winding-number sectors in x and y directions (W_x, W_y). The winding number commutes with the Hamiltonian and in the electric flux basis, the Hamiltonian is block diagonal. Out of a total of 18 states, 6 are in the zero-winding sector. The ground state lies in the zero-winding sector, and hence is characterized by a six-dimensional vector. Using the action of the Hamiltonian given in (20), the eigenvalues are obtained by diagonalizing the matrix

$$H_{(0,0)} = -J \begin{pmatrix} 0 & 1 & 0 & 0 & 1 & 0 \\ 1 & 0 & 1 & 1 & 0 & 1 \\ 0 & 1 & 0 & 0 & 1 & 0 \\ 0 & 1 & 0 & 0 & 1 & 0 \\ 1 & 0 & 1 & 1 & 0 & 1 \\ 0 & 1 & 0 & 0 & 1 & 0 \end{pmatrix}. \quad (\text{C1})$$

For $J = 1$, the eigenvalues are $-2.82843, 0, 0, 0, 0, 2.82843$.

Before doing a similar exercise with the fermionic version, we need to label our states according to a definite convention since fermionic operators are involved. The matrix which one obtains is

$$H_{(0,0)} = -J \begin{pmatrix} 0 & 1 & 0 & 0 & -1 & 0 \\ 1 & 0 & 1 & -1 & 0 & -1 \\ 0 & 1 & 0 & 0 & -1 & 0 \\ 0 & -1 & 0 & 0 & 1 & 0 \\ -1 & 0 & -1 & 1 & 0 & 1 \\ 0 & -1 & 0 & 0 & 1 & 0 \end{pmatrix}. \quad (\text{C2})$$

Indeed, on diagonalizing matrix (C2) we recover the same spectrum as that of (C1) for the quantum spin model.

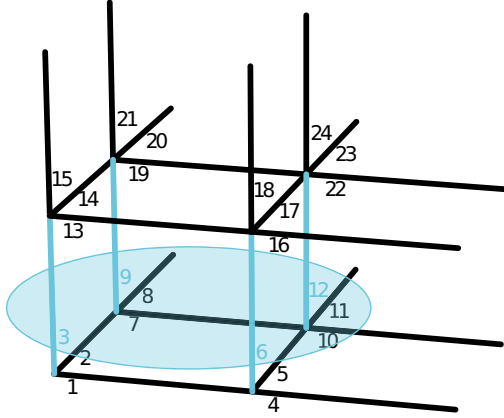


FIG. 15. Numbering of links on a $2 \times 2 \times 2$ lattice. The blue colored links [3, 6, 9, 12] are summed to obtain the total flux W_z in the z direction, indicated as the flux through a closed loop around the system in the z plane. Accordingly, W_x is obtained by summing the links [1, 7, 13, 19] and W_y via summation of the links [2, 5, 14, 17].

APPENDIX D: EXCHANGE OF TWO FERMIONS IN 3D

In this Appendix, we show the exact calculation demonstrating the emergence of a sign in the fermionic QLM, as argued in the main text (cf. Fig. 6, we write mathematically the flips that were considered in that figure). To do this, we first need to introduce the conventions regarding the ordering of operators, such that we are able to properly identify an overall sign. In our conventions, *normal ordering* refers to creation operators arranged so that their index is ascending from right to left, i.e., those with lower index are applied first.

Although the specific numbering of link variables merely is a technical detail, we show our convention in Fig. 15 for the sake of completeness. In this convention, the initial state discussed in the main text corresponds to

$$|\psi_0\rangle = c_{24}^\dagger c_{12}^\dagger c_{11}^\dagger c_{10}^\dagger c_7^\dagger c_5^\dagger c_4^\dagger c_1^\dagger |0\rangle. \quad (\text{D1})$$

Moreover, we denote the plaquette operators as

$$U_\square(i, j, k, l) = c_i^\dagger c_j^\dagger c_k c_l, \quad (\text{D2})$$

$$U_\square^\dagger(i, j, k, l) = c_i c_j c_k^\dagger c_l^\dagger, \quad (\text{D3})$$

where the indices denote the links of the plaquette in question.

With this, we are able to explicitly show the emergence of a sign for the example discussed in the main text, specifically the string of plaquette operators applied in Fig. 6(b). For the sake of brevity, we only consider explicitly the application of the first of six plaquette operators, namely,

$$\begin{aligned} |\psi_1\rangle &= U_\square^\dagger(5, 12, 17, 6)|\psi_0\rangle \\ &= [c_5 c_{12} c_{17}^\dagger c_6^\dagger] [c_{24}^\dagger c_{12}^\dagger c_{11}^\dagger c_{10}^\dagger c_7^\dagger c_5^\dagger c_4^\dagger c_1^\dagger |0\rangle] \\ &= c_{24}^\dagger c_{17}^\dagger c_{11}^\dagger c_{10}^\dagger c_7^\dagger c_6^\dagger c_4^\dagger c_1^\dagger |0\rangle, \end{aligned} \quad (\text{D4})$$

where the last line is obtained by exploiting the usual fermionic anticommutation relations. The subsequent operators generate the following sequence of states:

$$\begin{aligned} |\psi_2\rangle &= U_\square^\dagger(1, 6, 13, 3)|\psi_1\rangle \\ &= -c_{24}^\dagger c_{17}^\dagger c_{13}^\dagger c_{11}^\dagger c_{10}^\dagger c_7^\dagger c_4^\dagger c_3^\dagger |0\rangle, \end{aligned} \quad (\text{D5})$$

$$\begin{aligned} |\psi_3\rangle &= U_\square^\dagger(13, 17, 19, 14)|\psi_2\rangle \\ &= -c_{24}^\dagger c_{19}^\dagger c_{14}^\dagger c_{11}^\dagger c_{10}^\dagger c_7^\dagger c_4^\dagger c_3^\dagger |0\rangle, \end{aligned} \quad (\text{D6})$$

$$\begin{aligned} |\psi_4\rangle &= U_\square(2, 9, 14, 3)|\psi_3\rangle \\ &= -c_{24}^\dagger c_{19}^\dagger c_{11}^\dagger c_{10}^\dagger c_9^\dagger c_7^\dagger c_4^\dagger c_2^\dagger |0\rangle, \end{aligned} \quad (\text{D7})$$

$$\begin{aligned} |\psi_5\rangle &= U_\square(1, 5, 7, 2)|\psi_4\rangle \\ &= -c_{24}^\dagger c_{19}^\dagger c_{11}^\dagger c_{10}^\dagger c_9^\dagger c_5^\dagger c_4^\dagger c_1^\dagger |0\rangle, \end{aligned} \quad (\text{D8})$$

$$\begin{aligned} |\psi_6\rangle &= U_\square(7, 12, 19, 9)|\psi_5\rangle \\ &= -c_{24}^\dagger c_{12}^\dagger c_{11}^\dagger c_{10}^\dagger c_7^\dagger c_5^\dagger c_4^\dagger c_1^\dagger |0\rangle = -|\psi_0\rangle. \end{aligned} \quad (\text{D9})$$

As is evident from the last line, the application of these six operators (in this specific order) maps the state back to itself but with a sign that distinguishes a system with bosonic link variables from its fermionic counterpart.

-
- [1] K. G. Wilson, Confinement of quarks, *Phys. Rev. D* **10**, 2445 (1974).
- [2] F. Wilczek, Quantum chromodynamics: The modern theory of the strong interaction, *Annu. Rev. Nucl. Part. Sci.* **32**, 177 (1982).
- [3] J. Kogut and L. Susskind, Hamiltonian formulation of Wilson's lattice gauge theories, *Phys. Rev. D* **11**, 395 (1975).
- [4] M. C. Bañuls, R. Blatt, J. Catani, A. Celi, J. I. Cirac, M. Dalmonte, L. Fallani, K. Jansen, M. Lewenstein, S. Montangero *et al.*, Simulating lattice gauge theories within quantum technologies, *Eur. Phys. J. D* **74**, 165 (2020).
- [5] D. Horn, Finite matrix models with continuous local gauge invariance, *Phys. Lett. B* **100**, 149 (1981).
- [6] P. Orland and D. Rohrlich, Lattice gauge magnets: Local isospin from spin, *Nucl. Phys. B* **338**, 647 (1990).
- [7] S. Chandrasekharan and U. J. Wiese, Quantum link models: A discrete approach to gauge theories, *Nucl. Phys. B* **492**, 455 (1997).
- [8] R. Brower, S. Chandrasekharan, and U. J. Wiese, QCD as a quantum link model, *Phys. Rev. D* **60**, 094502 (1999).
- [9] H. Singh and S. Chandrasekharan, Qubit regularization of the $o(3)$ sigma model, *Phys. Rev. D* **100**, 054505 (2019).
- [10] H. Liu and S. Chandrasekharan, Qubit regularization and qubit embedding algebras, *Symmetry* **14**, 305 (2022).
- [11] S. A. Kivelson, D. S. Rokhsar, and J. P. Sethna, Topology of the resonating valence-bond state: Solitons and high- T_c superconductivity, *Phys. Rev. B* **35**, 8865 (1987).
- [12] R. Moessner and K. S. Raman, *Quantum Dimer Models* (Springer, Berlin, 2010), pp. 437–479.

- [13] R. Moessner and S. L. Sondhi, Three-dimensional resonating-valence-bond liquids and their excitations, *Phys. Rev. B* **68**, 184512 (2003).
- [14] D. Banerjee, F. J. Jiang, P. Widmer, and U. J. Wiese, The $(2+1)$ -d $U(1)$ quantum link model masquerading as deconfined criticality, *J. Stat. Mech.: Theory Exp.* (2013) P12010.
- [15] D. Banerjee, M. Bögli, C. P. Hofmann, F.-J. Jiang, P. Widmer, and U.-J. Wiese, Interfaces, strings, and a soft mode in the square lattice quantum dimer model, *Phys. Rev. B* **90**, 245143 (2014).
- [16] M. Hermele, M. P. A. Fisher, and L. Balents, Pyrochlore photons: The $U(1)$ spin liquid in a $S = \frac{1}{2}$ three-dimensional frustrated magnet, *Phys. Rev. B* **69**, 064404 (2004).
- [17] A. Banerjee, S. V. Isakov, K. Damle, and Y. B. Kim, Unusual Liquid State of Hard-Core Bosons on the Pyrochlore Lattice, *Phys. Rev. Lett.* **100**, 047208 (2008).
- [18] O. Sikora, F. Pollmann, N. Shannon, K. Penc, and P. Fulde, Quantum Liquid with Deconfined Fractional Excitations in Three Dimensions, *Phys. Rev. Lett.* **103**, 247001 (2009).
- [19] O. Sikora, N. Shannon, F. Pollmann, K. Penc, and P. Fulde, Extended quantum $u(1)$ -liquid phase in a three-dimensional quantum dimer model, *Phys. Rev. B* **84**, 115129 (2011).
- [20] D. Banerjee, M. Bögli, M. Dalmonte, E. Rico, P. Stebler, U. J. Wiese, and P. Zoller, Atomic Quantum Simulation of $U(N)$ and $SU(N)$ Non-Abelian Lattice Gauge Theories, *Phys. Rev. Lett.* **110**, 125303 (2013).
- [21] M. Troyer and U.-J. Wiese, Computational Complexity and Fundamental Limitations to Fermionic Quantum Monte Carlo Simulations, *Phys. Rev. Lett.* **94**, 170201 (2005).
- [22] B. Schliittgen and U.-J. Wiese, Low-energy effective theories of quantum spin and quantum link models, *Phys. Rev. D* **63**, 085007 (2001).
- [23] T. V. Zache, M. Van Damme, J. C. Halimeh, P. Hauke, and D. Banerjee, Achieving the continuum limit of quantum link lattice gauge theories on quantum devices, [arXiv:2104.00025](https://arxiv.org/abs/2104.00025).
- [24] C. Lanczos, An iteration method for the solution of the eigenvalue problem of linear differential and integral operators, *J. Res. Natl. Bur. Stand.* **45**, 255 (1950).
- [25] T. Matsubara and H. Matsuda, A Lattice Model of Liquid Helium, I, *Prog. Theor. Phys.* **16**, 569 (1956).
- [26] J. Bonča, S. Maekawa, and T. Tohyama, Numerical approach to the low-doping regime of the $t-j$ model, *Phys. Rev. B* **76**, 035121 (2007).
- [27] T. Grining, M. Tomza, M. Lesiuk, M. Przybytek, M. Musiał, P. Massignan, M. Lewenstein, and R. Moszynski, Many interacting fermions in a one-dimensional harmonic trap: a quantum-chemical treatment, *New J. Phys.* **17**, 115001 (2015).
- [28] P. Sala, T. Rakovszky, R. Verresen, M. Knap, and F. Pollmann, Ergodicity Breaking Arising from Hilbert Space Fragmentation in Dipole-Conserving Hamiltonians, *Phys. Rev. X* **10**, 011047 (2020).
- [29] S. Moudgalya, B. A. Bernevig, and N. Regnault, Quantum many-body scars and hilbert space fragmentation: A review of exact results, *Rep. Prog. Phys.* **85**, 086501 (2022).
- [30] B. Mukherjee, D. Banerjee, K. Sengupta, and A. Sen, Minimal model for hilbert space fragmentation with local constraints, *Phys. Rev. B* **104**, 155117 (2021).
- [31] F. Tschirsich, S. Montangero, and M. Dalmonte, Phase diagram and conformal string excitations of square ice using gauge invariant matrix product states, *SciPost Phys.* **6**, 028 (2019).
- [32] R. M. Nandkishore and M. Hermele, Fractons, *Annu. Rev. Condens. Matter Phys.* **10**, 295 (2019).
- [33] T. Felser, S. Notarnicola, and S. Montangero, Efficient Tensor Network Ansatz for High-Dimensional Quantum Many-Body Problems, *Phys. Rev. Lett.* **126**, 170603 (2021).
- [34] M. S. J. Tepaske and D. J. Luitz, Three-dimensional isometric tensor networks, *Phys. Rev. Research* **3**, 023236 (2021).
- [35] G. Magnifico, T. Felser, P. Silvi, and S. Montangero, Lattice quantum electrodynamics in $(3+1)$ -dimensions at finite density with tensor networks, *Nat. Commun.* **12**, 3600 (2021).
- [36] P. Zanardi and N. Paunković, Ground state overlap and quantum phase transitions, *Phys. Rev. E* **74**, 031123 (2006).
- [37] L. D'Alessio, Y. Kafri, A. Polkovnikov, and M. Rigol, From quantum chaos and eigenstate thermalization to statistical mechanics and thermodynamics, *Adv. Phys.* **65**, 239 (2016).
- [38] W.-L. You, Y.-W. Li, and S.-J. Gu, Fidelity, dynamic structure factor, and susceptibility in critical phenomena, *Phys. Rev. E* **76**, 022101 (2007).
- [39] L. Wang, Y.-H. Liu, J. Imriška, P. N. Ma, and M. Troyer, Fidelity Susceptibility Made Simple: A Unified Quantum Monte Carlo Approach, *Phys. Rev. X* **5**, 031007 (2015).
- [40] S.-J. Gu, Fidelity approach to quantum phase transitions, *Int. J. Mod. Phys. B* **24**, 4371 (2010).
- [41] F. Alet and N. Laflorencie, Many-body localization: An introduction and selected topics, *C. R. Phys.* **19**, 498 (2018).
- [42] D. González-Cuadra, E. Zohar, and J. I. Cirac, Quantum simulation of the abelian-higgs lattice gauge theory with ultracold atoms, *New J. Phys.* **19**, 063038 (2017).
- [43] J. Bender, E. Zohar, A. Farace, and J. I. Cirac, Digital quantum simulation of lattice gauge theories in three spatial dimensions, *New J. Phys.* **20**, 093001 (2018).
- [44] R. Ott, T. V. Zache, F. Jendrzejewski, and J. Berges, Scalable Cold-Atom Quantum Simulator for Two-Dimensional QED, *Phys. Rev. Lett.* **127**, 130504 (2021).
- [45] E. Guardado-Sanchez, B. M. Spar, P. Schauss, R. Belyansky, J. T. Young, P. Bienias, A. V. Gorshkov, T. Iadecola, and W. S. Bakr, Quench Dynamics of a Fermi Gas with Strong Nonlocal Interactions, *Phys. Rev. X* **11**, 021036 (2021).
- [46] U.-J. Wiese, From quantum link models to d-theory: A resource efficient framework for the quantum simulation and computation of gauge theories, *Philos. Trans. A. Math. Phys. Eng. Sci.* **380**, 20210068 (2021).